

# Modeling of wave propagation in polycrystalline ice with hierarchical density gradients

Farshad Ghanbari <sup>a</sup>, Eduardo G. Rodriguez <sup>b</sup>, Daniel Millán <sup>b</sup>, Francesco Simonetti <sup>c</sup>,  
Andrea P. Argüelles <sup>a</sup>, Christian Peco <sup>a,\*</sup>

<sup>a</sup> Department of Engineering Science and Mechanics, Penn State, University Park, 16802, PA, USA

<sup>b</sup> CONICET and Facultad de Ciencias Aplicadas a la Industria, Universidad Nacional de Cuyo, San Rafael, 5600, Mendoza, Argentina

<sup>c</sup> Department of Aerospace Engineering and Engineering Mechanics, University of Cincinnati, Cincinnati, 45221, OH, USA

## ARTICLE INFO

### Keywords:

Ice mechanics  
Attenuation  
Scattering  
Finite elements  
Statistical descriptors

## ABSTRACT

Polycrystalline solids are composed of many small grains of varying sizes and crystallographic orientations. An elastic wave that propagates through such a material experiences distortion and attenuation. While the influence on propagation in random configurations can be captured with conventional statistical descriptors, the role of second-order features such as the hierarchical gradient in material properties has not been explored. In this paper, we optimize a numerical strategy based on Finite Elements and Local Max-Entropy approximants to characterize the role of grain density gradients on ultrasonic attenuation. We focus on ice as a model for mesoscale ordered configurations due to its relevance to the emerging technology of cryoultronics. Our simulations in one- and two-dimensional settings indicate that second-order descriptors are required to predict attenuation in polycrystalline ice. Furthermore, we define a novel parameter, based on the standard deviation of the speed of sound gradient distribution, which shows a quadratic relationship with the ultrasonic attenuation. The model results can be understood as a phase diagram for the design of metamaterials with specific ultrasonic scattering properties.

## 1. Introduction

Polycrystalline materials exhibit a microstructure made of grains with various sizes, shapes, and crystallographic orientations. Wave propagation behavior through such a medium exhibits distortions that are highly dependent on the spatial statistics of the microstructure, whose descriptors must be chosen carefully in order to make predictions [1,2]. While we have descriptors to predict wave propagation response in conventional microstructures (e.g., average properties or two-point correlation functions in configurations that allow homogenization), the problem is more challenging with materials that exhibit a higher degree of ordering at the mesoscale. These hierarchically organized structures can occur in both natural and artificial materials, such as in ice freezing processes [3], metal forming [4,5], and soft matter and biological arrangements [6–8]. Interestingly, the study of wave propagation in ice has recently become relevant to ultrasonic non-destructive evaluation (NDE) and other critical problems, such as aircraft icing [9], glacial ice [10] and planetary science [11]. Due to its relevance to these problems, its potential to display complex hierarchical orderings, and its relative simplicity for laboratory experiments, we choose ice as our polycrystalline material model. We emphasize

here that only recently the influence of gradient patterns has been noticed and accounted for in the literature, and that it always appears circumscribed to a different family of features (e.g., microstructural defects [12]). The development of useful microstructural descriptors in the types of hierarchically ordered configurations is fundamental for the prediction of the wave propagation response in the aforementioned materials, which is of interest to scientists and engineers.

In this work, we focus our study on the attenuation response of an ultrasonic wave propagating through a (macroscopically isotropic) polycrystalline ice microstructure. As it progresses, the wave experiences reflection and refraction at the grain boundaries, leading to scattering. In consequence, the energy is spatially redistributed and the wave displays macroscopic attenuation and distortion [13–16]. Due to its importance, a number of studies in literature have characterized and evaluated wave propagation for different microstructures [17–22]. Nevertheless, when the polycrystal presents certain complexity (e.g., of crystallographic orientation, size, shape...), the models struggle to remain practical while incorporating a detailed description of the microstructural features. In consequence, these models are forced to introduce simplifications, hence achieving only approximate solutions.

\* Corresponding author.

E-mail address: [christian.peco@psu.edu](mailto:christian.peco@psu.edu) (C. Peco).

<https://doi.org/10.1016/j.finel.2023.103916>

Received 7 October 2022; Received in revised form 17 December 2022; Accepted 21 January 2023

Available online 29 January 2023

0168-874X/© 2023 Elsevier B.V. All rights reserved.

With the gradual increase of computational power, numerical methodologies that remove those simplifications have been put forward. The Finite Element Method (FEM) has been successfully applied to simulate and understand the scattering of elastic waves in polycrystalline solids [23–25]. A precise description of their performance and a comparison with analytical strategies based on statistical descriptors has been recently explored [26,27]. The aforementioned works primarily rely on synthetic polycrystals constructed through Voronoi [25,28,29] and non-Voronoi tessellations [30,31], with varying descriptors on the size and shape of the grains. However, the traditional focus on materials with random crystallographic orientations leaves aside materials with higher levels of organization (e.g., involving a gradient hierarchy at the mesoscale), which we address in our analysis. Additionally, the computational modeling of the phenomenon is still quite resource-intensive and can benefit from the refinement of the numerical approach. In this work, we also include a detailed study on the optimal strategy to simulate ultrasonic propagation in hierarchically ordered configurations in ice using both traditional FEM and Local-Max Entropy approximants (LME) [32], an advanced meshfree discretization method.

To further motivate the choice of ice and the ultrasonic range as our focus, we want to point out that the way ultrasonic waves are attenuated is highly relevant, for example, for NDE techniques, which play a vital role in the development and implementation of safety-critical components. Ultrasonic waves propagate and interact with internal features, such as pores, cracks, inclusions, and other microstructural defects [33–36] and the received signal can be used in conjunction with analytical and/or numerical models to deduce this information. In relation to ice, cryoultrasonic NDE has recently emerged as a solution for the inspection of components with complex geometries [37,38]. In this novel technique, the piece is embedded in ice to obtain an ideal sonic shape (i.e., a shape with rectilinear contours and ice-filled channels and voids). As a couplant material, ice closely matches the part's acoustic properties, leading to more adequate part-couplant interfaces. Ice is a polycrystalline material with the particularity of having a microstructure whose grain size distribution ranges in the ultrasonic wavelength. In consequence, ultrasonic measurements in the stochastic region and approaching the geometric regime become feasible. Additionally, ice structure is greatly influenced by the freezing process parameters, which determine the size, orientation, and spatial configuration of the grains [39,40]. As a result, ultrasonic wave propagation in ice demands a deeper characterization of its microstructure. This makes ice a perfect model for the analysis of scattering behavior in hierarchical microstructures. Nevertheless, our results and conclusions should be of general validity on microstructures that share similar features.

The remainder of the paper is organized as follows. In Section 2 we introduce the formulation of the problem and the numerical details, which involves one and two-dimensional simulations. Our one-dimensional codes are based on FEM and LME. Our two-dimensional codes are based on MOOSE [41], a FEM implementation. Efficiency and optimization details, as well as studies for the choice of the study parameters, are given in this section. In Section 3 we study how random and organized grain configurations affect the attenuation of ultrasonic waves. We explore different frequencies and mechanical properties variations to show that a second-order descriptor of the density gradient distribution dictates the behavior of the propagating wave. We finish with some concluding remarks and future lines of work in Section 4.

## 2. Formulation and numerical methodology

We aim to simulate the elastodynamic time response of ice with an arbitrary microstructure subject to an ultrasonic pulse, enabling the study of the effect of crystallographic orientation and grain size on the

longitudinal attenuation coefficient,  $\alpha_L$ . The standard model for wave propagation [42,43] parts from the conservation of linear momentum

$$\rho \ddot{\mathbf{u}} - \nabla \cdot \boldsymbol{\sigma}(\mathbf{u}) = \mathbf{f}, \quad (1)$$

where  $\mathbf{u}$  is the displacement and  $\boldsymbol{\sigma}$  is the stress tensor. In particular, we assume we have an elastic media, described by the linear constitutive relation (Hooke's law)

$$\boldsymbol{\sigma}(\mathbf{u}) = \mathbf{C} : \boldsymbol{\epsilon}(\mathbf{u}), \quad \boldsymbol{\epsilon}(\mathbf{u}) = \frac{1}{2}(\nabla \mathbf{u} + \nabla \mathbf{u}^T) \quad (2)$$

between the stress  $\boldsymbol{\sigma}$  and the infinitesimal strain  $\boldsymbol{\epsilon}(\mathbf{u})$  tensors, and where  $\mathbf{C}$  is the elasticity tensor. For implementation purposes, we use Voigt notation to express the stress as

$$\boldsymbol{\sigma} = \{\sigma_{xx}, \sigma_{yy}, \sigma_{zz}, \sigma_{xy}, \sigma_{xz}, \sigma_{yz}\}^T, \quad (3)$$

for which the governing equations may be written as

$$\rho \ddot{\mathbf{u}} - \mathbf{D}^T \boldsymbol{\sigma}(\mathbf{u}) = \mathbf{f}, \quad (4)$$

$$\boldsymbol{\sigma}(\mathbf{u}) = \mathbf{C} \mathbf{D} \mathbf{u}, \quad (5)$$

where  $\mathbf{D}$  represents the differential operator, which can take the form

$$\mathbf{D} = \begin{bmatrix} \partial_x & 0 & 0 \\ 0 & \partial_y & 0 \\ 0 & 0 & \partial_z \\ \partial_y & \partial_x & 0 \\ \partial_z & 0 & \partial_x \\ 0 & \partial_z & \partial_y \end{bmatrix} \quad \text{or} \quad \mathbf{D} = \begin{bmatrix} \partial_x & 0 \\ 0 & \partial_y \\ \partial_y & \partial_x \end{bmatrix} \text{ in 2D.} \quad (6)$$

We can start from Eq. (4) to develop the variational formulation of the problem, by taking the scalar product of both sides of Eq. (1) with a test function  $\mathbf{v}$  and integrating by parts over the domain  $\Omega$ , obtaining

$$\frac{\partial^2}{\partial t^2} \int_{\Omega} \rho \mathbf{v} \cdot \mathbf{u} \, d\Omega + \int_{\Omega} \boldsymbol{\epsilon}(\mathbf{v}) \cdot (\mathbf{C} : \boldsymbol{\epsilon}(\mathbf{u})) \, d\Omega = \int_{\Omega} \mathbf{v} \cdot \mathbf{f} \, d\Omega \quad \forall \mathbf{v} \in H_0^1(\Omega)^d, \quad (7)$$

where  $d = 2$  or  $3$  and  $H_0^1 = \{\mathbf{u} \in L^2(\Omega) \mid \nabla \mathbf{u} \in L^2(\Omega) \text{ and } \mathbf{u}|_{\partial\Omega} = 0\}$ . From here we can proceed to the spatial discretization, which in our case will be particularized at implementation level with FEM or LME. For example, for FEM, and defining a number  $n_e$  of finite elements  $\Omega^e$  ( $\Omega = \bigcup_{e=1}^{n_e} \Omega_e$ ), the approximate solution may be written as

$$\tilde{\mathbf{u}}(\mathbf{x}, t) = \bigcup_{e=1}^{n_e} \tilde{\mathbf{u}}^e(\mathbf{x}, t), \quad \tilde{\mathbf{u}}^e(\mathbf{x}, t) = \sum_{j=1}^{n_{dof}} \tilde{\mathbf{u}}_j^e(t) \boldsymbol{\phi}_j^e(\mathbf{x}), \quad (8)$$

where the union operator denotes that  $\tilde{\mathbf{u}}$  is defined in  $\Omega$ ,  $\tilde{\mathbf{u}}(\mathbf{x}, \cdot) = \tilde{\mathbf{u}}^e(\mathbf{x}, \cdot)$  for any  $\mathbf{x} \in \Omega^e$ ,  $n_{dof}$  is the number of element degrees of freedom, and  $\boldsymbol{\phi}_j^e$  is the Lagrange interpolation vector function associated with the  $j$ th degree of freedom. The coefficients  $\tilde{\mathbf{u}}_j^e(t)$  are determined from the following Galerkin approximation of Eq. (7):

$$\frac{\partial^2}{\partial t^2} \int_{\Omega} \rho \mathbf{v} \cdot \tilde{\mathbf{u}} \, d\Omega + \int_{\Omega} \boldsymbol{\epsilon}(\mathbf{v}) \cdot (\mathbf{C} \mathbf{D} \tilde{\mathbf{u}}) \, d\Omega = \int_{\Omega} \mathbf{v} \cdot \mathbf{f} \, d\Omega \quad \forall \mathbf{v} \in \tilde{V}, \quad (9)$$

where  $\tilde{V}$  is the subspace of  $H_0^1(\Omega)^d$  of continuous piecewise-polynomial functions built from local functions  $\boldsymbol{\phi}_j^e(\mathbf{x})$ . After algebraic manipulations, Galerkin Eq. (7) are written as the system of ordinary differential equations:

$$\mathbf{M} \ddot{\mathbf{u}} + \mathbf{K} \mathbf{u} = \mathbf{0}, \quad (10)$$

in the absence of damping and externally applied forces. In Eq. (10)  $\mathbf{M}$  and  $\mathbf{K}$  are the global mass matrix and stiffness matrix, respectively. Initial conditions  $\mathbf{U}(0) = \mathbf{U}_0$  and  $\dot{\mathbf{U}}(0) = \dot{\mathbf{U}}_0$ , must be provided. They are built through a summation process of elemental matrices and vectors,

$$\mathbf{M} = \sum_{e=1}^{n_e} \mathbf{M}^e, \quad \mathbf{K} = \sum_{e=1}^{n_e} \mathbf{K}^e, \quad (11)$$

where  $\mathbf{M}^e$  and  $\mathbf{K}^e$  are the elemental mass matrix, and stiffness matrix and in sparse global form, that is, only non-zero entries are used and they are mapped into appropriate global locations by a connectivity

map from local to global nodes. The dense elemental arrays  $\mathbf{M}^e$  and  $\mathbf{K}^e$  are defined by the contributions from element  $\Omega_e$  to the integrals as

$$\mathbf{M}_{ij}^e = \int_{\Omega_e} \rho \boldsymbol{\phi}_i^e \cdot \boldsymbol{\phi}_j^e d\Omega, \quad \mathbf{K}_{ij}^e = \int_{\Omega_e} (\mathbf{D}\boldsymbol{\phi}_i^e) \cdot (\mathbf{C} \mathbf{D}\boldsymbol{\phi}_j^e) d\Omega, \quad (12)$$

for  $1 \leq i, j \leq n_{dof}$ . We then proceed to discretize in time using the Newmark [44] method. In the Newmark time integration scheme, the acceleration and velocity at  $t + \Delta t$  are written in terms of displacement, velocity, and acceleration at time  $t$  and the displacement at  $t + \Delta t$  using

$$\ddot{\mathbf{u}}(t + \Delta t) = \ddot{\mathbf{u}}(t) + \Delta t(1 - \gamma)\ddot{\mathbf{u}}(t) + \gamma\Delta t\ddot{\mathbf{u}}(t + \Delta t), \quad (13)$$

$$\dot{\mathbf{u}}(t + \Delta t) = \frac{\dot{\mathbf{u}}(t + \Delta t) - \dot{\mathbf{u}}(t)}{\beta\Delta t^2} - \frac{\ddot{\mathbf{u}}(t)}{\beta\Delta t} + \frac{\beta - 0.5}{\beta}\ddot{\mathbf{u}}(t), \quad (14)$$

where  $\dot{\mathbf{u}}$  and  $\ddot{\mathbf{u}}$  are the velocity and acceleration vectors, respectively. In Eqs. (13) and (14),  $\beta$  and  $\gamma$  are Newmark time integration parameters. Substituting the two equations in Eq. (10) results in a linear system of equations that has  $\ddot{\mathbf{u}}(t + \Delta t)$  as its only unknown. For all of our 1D and 2D simulations, we choose  $\beta = 0.25$  and  $\gamma = 0.5$  for which the Newmark time integration method is implicit and unconditionally stable with no numerical damping. In consequence, we ensure that the value of  $\alpha_L$ , the longitudinal attenuation coefficient, is not affected by the numerical damping due to the choice of the time integration scheme.

Finally, the choice of the wave pulse is particularly relevant, as our models must be able to correctly reproduce the high-frequency (MHz range) signals without loss or distortion. The sine function and the Hann-windowed tone burst are the most widely used in the field. For the type of numerical simulations in this study, our analysis concluded that the Hann-windowed tone burst is more suitable than the sine function. While the latter generates multiple reflections at the front of the signal that distort the received signal, the Hann-windowed achieves a clean, stable wave propagation. The signal takes the general form:

$$u(t) = h(t) \sin(2\pi f t), \quad (15)$$

where  $f$  is the pure tone burst frequency (center frequency) and  $h(t)$  is the Hann-windowed function defined by

$$h(t) = \frac{1}{2} \left[ 1 - \cos\left(\frac{2\pi t}{T_H}\right) \right], \quad (16)$$

where  $T_H$  is the Hann-windowed length, which can be calculated using the number of cycles in the tone burst signal  $N_B$  as

$$T_H = N_B / f. \quad (17)$$

## 2.1. One-dimensional spatial discretization: FEM and LME approximants

We use a 1D numerical model for the directional isolation and analysis of the grain configurations effects on wave propagation. The 1D setting allows us to efficiently explore the parameter space (size, material properties, and relative order of grains) and increase the number of realizations per simulation, hence ensuring statistical significance.

We define the base setting with an elastic bar of length  $L$ , as sketched in Fig. 1. We divide the domain into a collection of equal-sized longitudinal grains (main figure). Each grain is then numerically discretized with a one-dimensional grid of nodes (i.e., internal divisions shown at the zoomed-in grain panel). The average material properties for our simulations are the following [45]: Young's modulus  $E_s = 9$  GPa and density  $\rho = 916.8$  kg/m<sup>3</sup>. An elastic wave will thus propagate at velocity  $c = \sqrt{E_s/\rho}$ . The density of the grains (and therefore the speed of sound  $c$  and impedance) can be kept homogeneous along the bar for control simulations and then varied per grain to generate different polycrystalline structures. The bar contains 163 grains of equal size (0.6135 mm). To generate the wave, we apply a three-cycle Hann-windowed toneburst as a Dirichlet boundary condition on the left side  $x = 0$ . A typical problem uses lengths around 100 mm and frequencies from 3 to 7 MHz. We compare the amplitude of emitted and received signals at the extremes of the 1D domain. The numerical parameters

(e.g., number of nodes per wavelength, type of wave signal, time step) are chosen with strict convergence and optimization criteria as detailed in Section 2.3. Note that we define the number of elements per wavelength  $\lambda$  (and not per grain) because it is more restrictive for the values in this study.

The discretization alternatives that we present for 1D simulations are classical FEM first and second-order Lagrange polynomials (P1 and P2 elements), and LME approximants, a meshfree method. The interest in studying the behavior of LME approximants stems from the attractiveness of smooth basis functions in general for the numerical solution of PDEs. Some examples include B-splines, nonuniform rational B-splines (NURBS), and isogeometric analysis (IGA) [46,47]. The strength of IGA is in high-fidelity boundary representation, whereas its weakness is in realizing bulk discretizations; hence, using a more flexible, meshfree method in the bulk as LME or coupling it with IGA can resolve several numerical challenges [48]. The LME approximant schemes were developed in [32] using a framework similar to meshfree methods, which implies their trivial extension to 2D and 3D domains represented by a scattered set of points in contrast with B-splines, NURBS, and IGA. LME approximants have a Gaussian decay that is modulated by a nondimensional parameter  $\gamma_{LME}$ , which controls the aspect ratio and effective support of the resulting basis functions. As  $\gamma_{LME}$  tends to infinity, it has been proved [32] that the affine function supported on the Delaunay triangulation of the node set is recovered. In practice, for  $\gamma_{LME} = 4$  the shape functions are visually very close to the Delaunay approximant. In [32], it was shown that for some values of  $\gamma_{LME}$ , the approximation properties of the maximum-entropy basis functions are greatly superior to those of the finite element linear functions representing smooth solutions, even when the added computational cost due to larger support is taken into account. Subsequent studies show that maximum entropy shape functions are suitable for solving a variety of problems, such as linear [49] and geometrically nonlinear thin shell analysis [50], compressible and nearly incompressible elasticity problems, and large deformations in biomembranes [51,52]. The LME approximations have several advantages over other meshfree methods such as the element-free Galerkin method [53] or the reproducing kernel particle method [54], and are amenable for parallelization and supercomputing. For example, in contrast to the above-mentioned methods, LME approximations fulfill the weak Kronecker-delta properties facilitating the imposition of Dirichlet boundary conditions, their shape functions are always positive which leads to non-negative values in the off-diagonals in the mass matrix, and they require fewer integration points to achieve the same accuracy [55–57]. In all examples we use  $\gamma_{LME} = 1.8$ .

## 2.2. Two-dimensional spatial discretization and grain structure: MOOSE and NEPER implementation

We develop our computational framework in MOOSE (Multiphysics Object-Oriented Simulation Environment) [41], an open-source, parallel finite element implementation. The package is based on PETSc [58, 59], which ensures optimal scalability for the resolution of large scale problems in our supercomputer facility [60]. To create the tessellations in two-dimensional domains representing the microstructure, we employ Neper [61], an open-source polycrystal generation software.

To facilitate the comparison with 1D results and to isolate the effect of grain size distribution vs. grain shape, we use Neper's Lloyd algorithm. As shown in Fig. 2(a), this algorithm generates uniform centroidal Voronoi tessellations (CVT) to create a microstructure of high shape-wise regularity, which serves well the purpose of this study. The input sphericity and grain diameter histograms for this microstructure are displayed in Fig. 2(b) and (c). The sphericity of a polyhedron, according to Neper's documentation, is the ratio of the surface area of the sphere of equivalent volume to the surface area of the polyhedron. Clearly, in two dimensions, the sphericity measure corresponds to the ratio of the perimeter of the circle of equivalent surface area to the

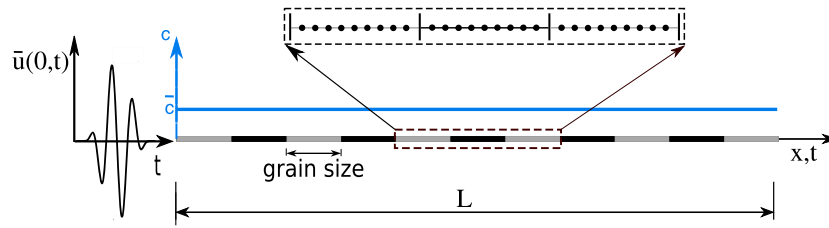


Fig. 1. Sketch of the computational domain used to represent the polycrystalline nature of ice. In the main figure, the domain is divided in equal-sized longitudinal grains. The magnified section shows how each grain is spatially discretized with a one-dimensional collection of nodes.

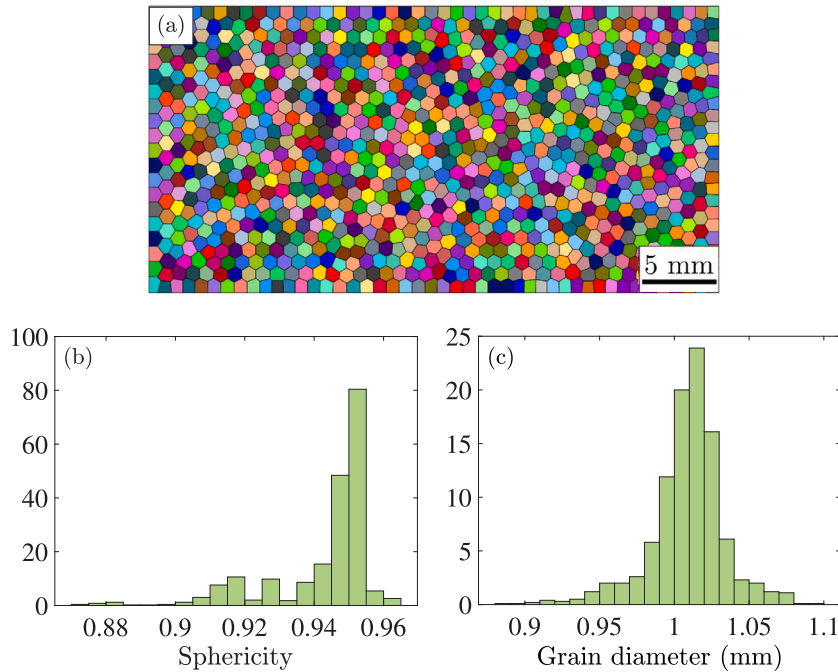


Fig. 2. (a) Example of the computational domain with uniform centroidal Voronoi tessellation, and its corresponding grain sphericity (b) and grain diameter (c) histograms. The vertical axis in histograms is normalized so that the data represents the probability density function estimate and the total number of grains for this example is 1000.

perimeter of the polygon. Note that we choose this algorithm because of the convenience for this work, but more advanced approaches are available to represent realistic microstructures, if needed [31,61]. Although traditionally standard Voronoi tessellations can be employed to represent microstructures with relative success [62–64], the so-called digital statistical twins approach streamlines the model fitting and validation process by bringing the synthetic microstructure as close as possible to the experimental microstructures. Digital microstructures that are statistically equivalent to real counterparts can be easily generated using Neper's grain growth algorithms. The analysis of such microstructures and their validation using real ice micrographs will be the subject of a subsequent study.

We impose symmetry boundary conditions (SBC) on the top and bottom edges of our domain to account for a quasi longitudinal plane wave in the horizontal direction  $x$ . SBCs can be implemented by setting the displacements in the direction perpendicular to the propagation direction, namely  $u_y$ , equal to zero. In the 2D case, it has been shown that, given a large enough sampling space in the simulation domain, SBCs and periodic boundary conditions perform equally well in capturing the plane wave solution in polycrystalline materials [65]. Furthermore, to generate the wave, we apply a three-cycle Hann-windowed toneburst as a Dirichlet boundary condition for  $u_x$  at  $x = 0$  (the transmitting surface).

In our simulations, the length and the height of the domain (i.e.,  $l_x$  and  $l_y$  in Fig. 3(a)), vary based on the mean grain diameter. More specifically, a larger mean grain diameter requires a larger domain size to ensure sufficient sampling space in the longitudinal and the transverse directions to accommodate for SBCs. It is worth mentioning that the grains near the top and the bottom boundaries get doubled in size due to the mirroring effect caused by the choice of the SBC. Choosing a sufficiently large enough domain is believed to average out the stronger scattering due to these larger boundary grains. The boundary at the rightmost side of the domain along  $l_y$  is kept traction-free.

The discretization of the computational domain is heavily influenced by two length scales present in the model, namely, the wavelength,  $\lambda$ , and the mean grain diameter,  $d$ . Based on the performance study we take in Section 2.3, we choose  $\lambda/h \geq 20$  and  $d/h \geq 10$ , where  $h$  is the mesh size. Furthermore, we employ structured meshes with quadrilateral elements. It has been shown that the choice of structured mesh compared to an unstructured conforming mesh does not affect the solution if the mesh is chosen to be fine enough to resolve the grain boundaries [65]. The choice of structured meshes will reduce the mesh density and, consequently, the computation time. Fig. 3(b) shows an example of the mesh that is used in our 2D simulations.



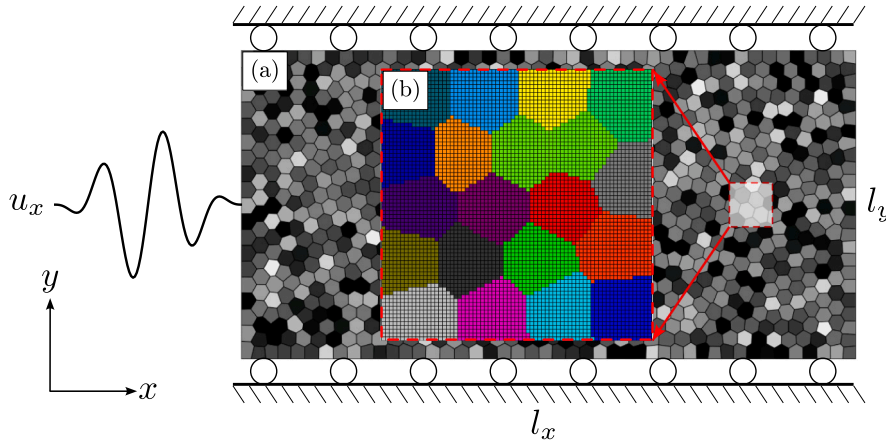


Fig. 3. Sketch of the computational domain used in 2D simulations. The symmetry boundary condition and the choice of input pulse is shown in (a) and (b) illustrates the structured mesh with quadrilateral elements used in this study.

We consider the following elastic stiffness of a single crystal with hexagonal symmetry reported in [66]:

$$\mathbf{C} = \begin{bmatrix} C_{11} & C_{12} & C_{12} & 0 & 0 & 0 \\ C_{12} & C_{22} & C_{23} & 0 & 0 & 0 \\ C_{12} & C_{23} & C_{22} & 0 & 0 & 0 \\ 0 & 0 & 0 & C_{44} & 0 & 0 \\ 0 & 0 & 0 & 0 & C_{55} & 0 \\ 0 & 0 & 0 & 0 & 0 & C_{55} \end{bmatrix}. \quad (18)$$

Eq. (18) describes all the elastic properties that are needed to assemble the global stiffness matrix  $\mathbf{K}$  in Eq. (10). The ice material properties used in this study including the mass density as well as the values of elastic constants in Eq. (18) are summarized in Table 1. For a polycrystalline microstructure, the 3D elastic stiffness matrix  $\mathbf{C}$  is rotated by a set of random Euler angles, assigned to each grain. We adopt the passive Bunge convention with  $Z_0, X_1, Z_2$  rotations in which we apply 3 successive rotations characterized by the Euler angles about the  $Z$  axis, then about the new  $X$  axis, and finally about the new  $Z$  axis. Here the axis subscripts 0, 1, and, 2 indicate the rotation occurrences. For a set of three Euler angles  $\theta_1, \theta_2, \theta_3$  the orthogonal rotation tensor becomes:

$$\mathbf{R}(\theta_1, \theta_2, \theta_3) = \begin{bmatrix} R_{11} & R_{12} & R_{13} \\ R_{21} & R_{22} & R_{23} \\ R_{31} & R_{32} & R_{33} \end{bmatrix}, \quad (19)$$

where

$$R_{11} = \cos \theta_1 \cos \theta_2 - \sin \theta_1 \sin \theta_2 \cos \theta_3 \quad (20)$$

$$R_{12} = \sin \theta_1 \cos \theta_2 + \cos \theta_1 \sin \theta_2 \cos \theta_3 \quad (21)$$

$$R_{13} = \sin \theta_2 \sin \theta_3 \quad (22)$$

$$R_{21} = -\cos \theta_1 \sin \theta_2 - \sin \theta_1 \cos \theta_2 \cos \theta_3 \quad (23)$$

$$R_{22} = -\sin \theta_1 \sin \theta_2 + \cos \theta_1 \cos \theta_2 \cos \theta_3 \quad (24)$$

$$R_{23} = \cos \theta_2 \sin \theta_3 \quad (25)$$

$$R_{31} = \sin \theta_1 \sin \theta_3 \quad (26)$$

$$R_{32} = -\cos \theta_1 \sin \theta_3 \quad (27)$$

$$R_{33} = \cos \theta_3. \quad (28)$$

Finally, we obtain the rotated elastic tensor as:

$$C_{ijkl} = R_{im} R_{jn} R_{ko} R_{lp} C_{mnop}, \quad (29)$$

where  $C_{mnop}$  is the unrotated rank four elastic tensor whose Voigt representation is defined in Eq. (18). The random crystallographic orientations have a uniform distribution to ensure macroscopic isotropy [26]. We then assume a plane strain formulation, in which the out-of-plane strain is set to zero. Consequently, the corresponding entries of the rotated  $\mathbf{C}$  are dropped out to accommodate the 2D formulation.

### 2.3. Convergence, wave pulse, and choice of optimal time step

In this study, we use both the traditional  $L_2$ -norm and the total energy as the quantities of interest to establish convergence. Considering  $\Omega$  as the one-dimensional domain through which the wave propagates, the total amount of energy is expressed as:

$$E = \frac{1}{2} \int_{\Omega} \left[ \left( \frac{\partial u}{\partial t} \right)^2 + c^2 \left( \frac{\partial u}{\partial x} \right)^2 \right] dx, \quad (30)$$

where the quadratic form  $E$  is constant over time and  $c^2 = E_s/\rho$ . The first and second terms in  $E$  are related to the kinetic and potential energies, respectively. As a reminder, the  $L_2$ -norm of the error is defined as:

$$\|e\|_{L_2} = \left( \int_{\Omega} |u - \tilde{u}|^2 dx \right)^{1/2}, \quad (31)$$

where  $\tilde{u}$  is a spatially discretized version of the continuous function  $u$  (i.e., using either FEM or LME). We use d'Alembert's general solution to obtain the exact solution  $u$  of the Hann-windowed signal, that is

$$u(x, t) = A \frac{1}{2} \left[ 1 - \cos \left( \frac{2\pi t}{T_H} - \frac{kx}{N_B} \right) \right] \sin(kx - 2\pi f t), \quad (32)$$

which we use to compute the  $L_2$ -norm error and the energy error of the numerical solution  $\tilde{u}$  at the end of the bar.

We first use these two convergence criteria to further justify the choice of the Hann-windowed wave pulse. We compare the behavior of a sinusoidal and a Hann-windowed pulse on the one-dimensional bar framework and average values presented in Section 2.1. The frequency of the pulses is set to 3.5 MHz and the domain is discretized with P1 FEM, using three integration Gauss points per element. Besides the visual absence of perturbations in the front of the Hann-windowed signal, Fig. 4 shows how this type of pulse consistently outperforms the sinusoidal signal both in (1) energy relative and  $L_2$ -norm errors, and (2) accuracy as the number of finite elements per grain increases. We can also observe how the Hann-windowed pulse achieves higher accuracy faster, which reduces the computational cost.

The choice of an adequate integration time step  $\Delta t$  is critical for the accuracy and convergence of the solution. A time step that is too small would render the computation time impractical. Conversely, using time steps that are too large hinders the resolution of high-frequency components. Although our scheme is unconditionally stable, a practical route to find an accurate time step is to apply a factor  $\chi$  on the expression [67]:

$$\Delta t \leq \chi \frac{\Delta x}{c}, \quad (33)$$

which is reminiscent of the Courant–Friedrichs–Lewy (CFL) condition [68] for the stability of explicit schemes, where  $\Delta x$  is the space

**Table 1**  
Ice material properties.

$\rho$ (kg m <sup>-3</sup> )	$C_{11}$ (GPa)	$C_{12}$ (GPa)	$C_{22}$ (GPa)	$C_{23}$ (GPa)	$C_{44}$ (GPa)	$C_{55}$ (GPa)
916.8	15.010	5.765	13.929	7.082	3.4235	3.014

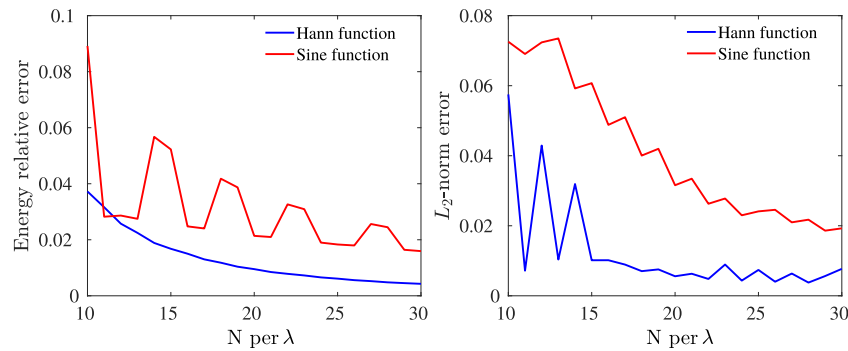


**Fig. 4.** Comparison of the two signals as an external force: Hann-windowed tone burst signal and sine function. On the left is the energy relative error and on the right is the  $L_2$ -norm error. The frequency of the pulses is set to 3.5 MHz and the domain is discretized with  $p = 1$  FEM, using three integration Gauss points per element,  $N_g = 3$ .

between two spatial discretization points and  $c$  is the wave speed. The factor  $\chi$  can be understood in the limit as the ratio of the traveled length per time step.

We now extensively analyze the convergence behavior of our models according to changes in (1) type of discretization method, (2) number of elements per wavelength, (3) time step  $\Delta t$  and coefficient  $\chi$ , and (4) number of Gauss points. Our objective is to justify an optimal selection of parameters for the computational setting used in our study, and establish the behavior of FEM and LME discretization methods as a reference for future applications. Again, we execute the simulations on the one-dimensional framework and average parameters specified in Section 2.1. Following the aforementioned results, we introduce a Hann-windowed pulse of 3.5 MHz and observe the evolution of the error when the objective parameters are modified. We summarize the most important results of our analysis in Figs. 5 and 6. In Fig. 5(a), we study how the  $L_2$ -norm error behaves varying  $\chi$  between 0.1 and 0.9 as the number of elements per wavelength ( $N$  per  $\lambda$ ) is increased. We present this variation for different discretization methods and number of Gauss points: FEM P1 element integrated with three Gauss points, FEM P2 element with five Gauss points, and LME with five Gauss points. The Gauss points number ( $N_g$ ) for each basis function is such that optimizes integration accuracy and computational cost. We observe relevant values around  $\chi = 0.47$  and  $\chi = 0.7$ , and we further analyze and make comparisons in Fig. 5(b) and (c), respectively. The comparison in Fig. 5(b) confirms how the three methods achieve more accurate and stable solutions as the number of elements per grain increases. Interestingly, LME is extremely smooth at all levels of discretization, while P1 oscillates in coarse meshes and only consolidates at the 20 elements threshold. In contrast, P2 has a much more steep convergence and achieves higher accuracy with fewer elements.

This prevalence of P2 is repeatable for other values of  $\chi$  and would point to this discretization element as the most appropriate one. However, a detailed analysis for a larger range of  $\chi$ , that we present in Fig. 6(a), confirms that the minimum observed in Fig. 5(a) around  $\chi = 0.7$  exists for different number of elements per wavelength, at which P1 outclasses the other methods. Interestingly, the same study for LME with  $\gamma_{LME} = 1.8$  in Fig. 6(b) reveals that LME decreases the error monotonically as  $\chi$  is decreased, and for different number of elements  $N$  per  $\lambda$ . This would be recommended for applications in which the reduction of the time step is required and therefore the monotonic, predictable behavior of the error is an advantage. For the relatively simple setting of our study, we fix  $\chi = 0.7$  and we select P1 and at least 20 elements per wavelength to ensure proper convergence and optimal performance.

### 3. Numerical results and discussion

In this section, we apply our numerical model to calculate attenuation in ice, which serves as a model for polycrystalline material wave propagation. We introduce the way we compute attenuation and then we (1) explore attenuation vs. grain size and compare it with homogenization analytical techniques, (2) study the role of hierarchical distributions and second-order descriptors in 1D, and (3) analyze and test the role of the standard deviation of density gradients in a more realistic 2D setting.

#### 3.1. Ultrasonic attenuation

We calculate the attenuation coefficient  $\alpha_L$  following the method suggested by Kalashnikov [69]. In general, the change of amplitude  $A$  of a decaying/attenuating plane wave can be expressed as:

$$A = A_0 e^{-\alpha_L d_p}, \quad (34)$$

where  $A_0$  is the transmitted amplitude of the propagating wave and  $d_p$  is the traveled distance from the initial location (propagation length).  $\alpha_L$  is expressed here as Np/m. To this extent, the fast Fourier transform of the time domain for the transmitted and received signals is calculated.

Then the attenuation coefficient is obtained by comparing the frequency domain of the transmitted and the received signals at each frequency (see Fig. 7(b)). The transmitted signal is readily available at  $l_x = 0$ . The received signal is calculated at the propagation length,  $d_p$ , which is taken to be at 90% of the domain length,  $l_x$ . In order to evaluate the received signal in the two-dimensional case, we sample a line at  $d_p$  consisting of 1000 discrete points along the width of the domain  $l_y$ . At each time step, this generates a displacements vector of dimension 1000, which is averaged to get the final form of the received signal. Fig. 7 clearly shows the loss of amplitude of the propagating wave at  $d_p$ .

#### 3.2. Influence of grain size and frequency in numerical and analytical attenuation

In this section, we study the role of average grain size and frequency on the attenuation behavior. Our simulations are performed on quasi-uniform grain size distributions (i.e., Gaussian with a very small standard deviation) and a random rotation pattern of the grain elasticity tensor. We compare our results to Weaver's theory of wave

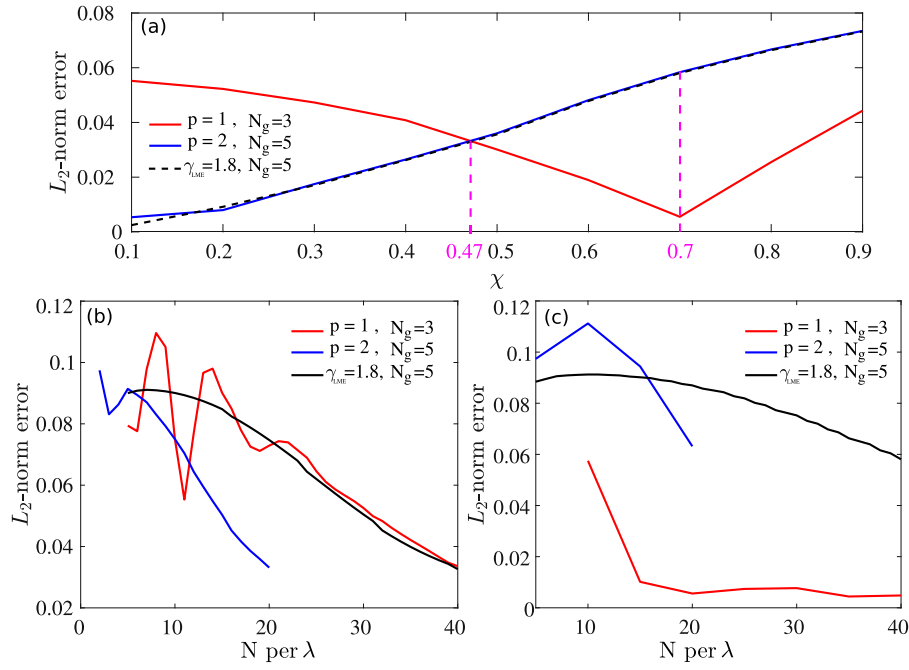


**Fig. 5.** (a)  $L_2$ -norm error for P1, P2 and LME for 40 elements. (b)  $L_2$ -norm error at  $\chi = 0.47$  and for different number of elements per wavelength,  $N$  per  $\lambda$ . (c)  $L_2$ -norm error at  $\chi = 0.7$  and for different  $N$  per  $\lambda$ .

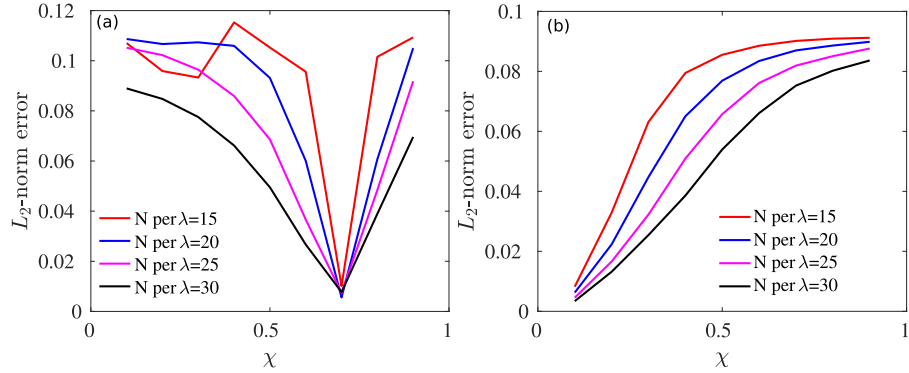


**Fig. 6.**  $L_2$ -norm error as a function of the number of elements per wavelength, varying  $\chi$  between 0.1 and 0.9 for discretizations (a) FEM,  $p=1, N_g=3$ , and (b) LME,  $\gamma_{LME}=1.8, N_g=5$ .

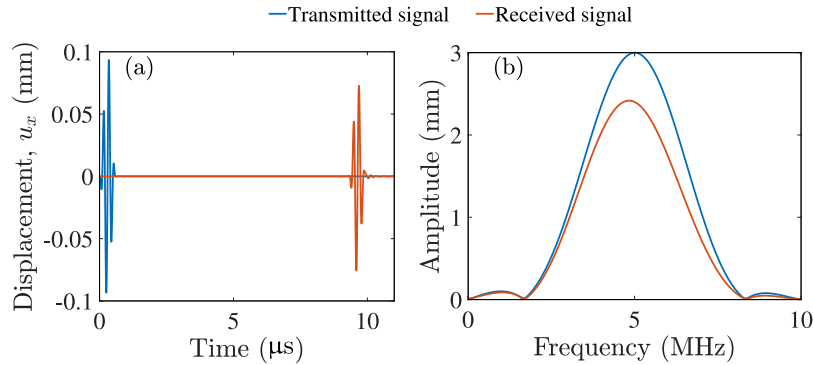


**Fig. 7.** Typical (a) time and (b) frequency domains for the transmitted signal and received 5 MHz center frequency signal corresponding to Model I defined in Table 2. The amplitude decrease is clearly visible in both time and frequency domain plots.

propagation in polycrystals [14]. Weaver's theoretical model was evaluated using the single crystal elastic constants in Table 1 (Section 2.2) and is valid through the stochastic regime. Although the theory is formulated in 3D, for the scattering regime that we are considering in

this study, it was shown that the 2D model performs as well as the 3D one in recovering the theory [70]. Therefore, we did not modify the theory to accommodate our 2D simulations. For the comparison, we have considered different mean grain diameters in the range of 67  $\mu m$  to

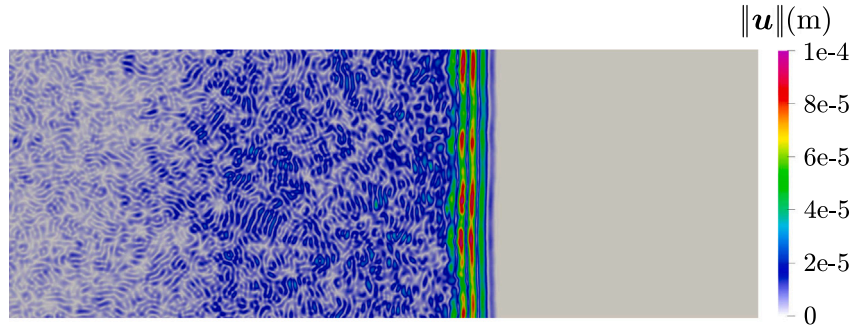


Fig. 8. Snapshot of the ultrasonic wave propagation in random uniform microstructure corresponding to 5 MHz center frequency and 67  $\mu\text{m}$  average grain diameter taken at  $t = 7 \mu\text{s}$ . The color bar represents the magnitude of the displacement.

Table 2

Details of the models used for the attenuation simulations in 2D.  $n$ ,  $d$ ,  $h$ , DOF,  $f$ , and R are the total number of grains, mean grain diameter, element size, number of degrees of freedom, center frequency, and number of realizations, respectively.

Model name	$l_x \times l_y$ (mm <sup>2</sup> )	$n$	$d$ (mm)	$h$ (mm)	DOF	$f$ (MHz)	R
I	$10 \times 2.5$	5,513	0.0669	0.006	1,393,057		
II	$10 \times 5$	5,000	0.113	0.01	1,003,002		
III	$12 \times 10$	3,000	0.220	0.02	602,202	3.5, 5	15
IV.A	$20 \times 20$	4,489	0.336	0.03	892,448		
IV.B		1,089	0.684				

680  $\mu\text{m}$  for 3.5 and 5 MHz center frequencies. Due to the random nature of the wave scattering, it is required to perform a statistical analysis of multiple microstructures that are randomly generated. Achieving statistical significance implies the generation of random grain geometries as well as random crystallographic orientations. However, producing and meshing unique random distributions is computationally expensive. To mitigate the time demands of this process, we follow the strategy presented in [65]. It has been shown that multiple random microstructure realizations can be achieved using a faster approach in which the grain geometries are kept unchanged and only the crystal orientations, represented by Euler angles, are randomly re-assigned. Van Pamel et al. [65] report that the results are statistically equivalent to those from randomly changing the grain structures and the crystal orientations.

Fig. 8 shows an example of the simulated wavefront propagation and the corresponding scattering. The color bar represents the magnitude of the displacement in m, and the snapshot is taken at  $t = 7 \mu\text{s}$ . The distortion of the wavefront, as well as the reflection of the wave inside the medium, are clearly visible in Fig. 8. We have considered 15 realizations corresponding to the grain diameters shown in Fig. 9(a). Each realization is characterized by a set of random Euler angles that rotate the elasticity tensor of the individual grains. We then calculate the corresponding attenuation coefficient  $\alpha_L$  using the methodology explained in Section 3.1. Details of the models used for this study are listed in Table 2.

In accordance with the analytical model, we observe that for both 3.5 and 5 MHz center frequencies the attenuation coefficient increases with the mean grain diameter up to the 330  $\mu\text{m}$  threshold. Interestingly, the same is not true for the mean grain diameters larger than 330  $\mu\text{m}$ , as shown in Fig. 9(a). Over that threshold (i.e., grain diameters larger than 330  $\mu\text{m}$ ),  $\alpha_L$  reaches a plateau, which can further be explained as the transitional scattering zone between the Rayleigh and the stochastic scattering regimes. The transitional zone can be visualized (see Fig. 9(b)) by plotting the normalized attenuation  $\alpha_L d$  versus normalized propagation constant  $kd$  in the log space, where  $d$  is the grain diameter and  $k$  represents the wave number. As shown in Fig. 9(b), the transitional zone marks the end of the Rayleigh scattering regime and the beginning of the stochastic scattering regime for which  $kd \ll 1$  and  $kd \gg 1$ , respectively.

The steep section of each curve in Fig. 9(a) represents the increase of sensitivity of a particular wavelength to the mean grain size. Attenuation values close to zero correspond to grain diameters that cannot be detected by the comparatively large wavelength. As the grain size increases, so does the attenuation. As expected, the higher frequency with a shorter wavelength is more sensitive to the smaller diameters and shows, in general, more attenuation. The finite element results reported in this section show good agreement with the theory, exhibiting an average relative difference of 13.7%. Note that we have used the average grain diameter in our analytical model for comparison. The results are comparable to other studies in literature, but the use of the two-point correlation function of real microstructures can significantly reduce this difference [71]. The results depicted in Fig. 9(a) and (b) are relevant for the validation of the numerical model and for the selection of frequencies and grain diameters, as well as giving a first approximation to the attenuation behavior in polycrystalline ice.

### 3.3. Role of interface gradient of grain distribution in attenuation

In this section, we study how the attenuation varies when the density of the ice grains is modified, following both natural and artificial configurations. Our objective is to capture the governing statistical parameters and study the role of second-order descriptors in uncommon grain arrangements. We frame the problem on a one-dimensional domain to initially isolate a single longitudinal response. We extend this study to two-dimensions in Section 3.4. An example of the one-dimensional setting we use is shown in Fig. 10. We introduce changes of density in the grains and therefore we affect the speed of sound  $c$  (and therefore impedance). We apply a three-cycle Hann-windowed toneburst as a Dirichlet boundary condition on the left side  $x = 0$  and use the numerical scheme presented in Section 2.1 with P1 FEM. The results are consistent with those obtained by applying LME. To standardize the numerical simulations and avoid local effects, we compare the amplitude of emitted and received signals at the extremes of the 1D domain, where the speed of sound is kept constant. Between those measuring extremes, 163 grains of equal size (0.6135 mm) are placed, mimicking a filter. The material property distributions of grains are realized through a vector of speeds  $c$  with 163 different values of speed, whose variability stems from changes in density. The density



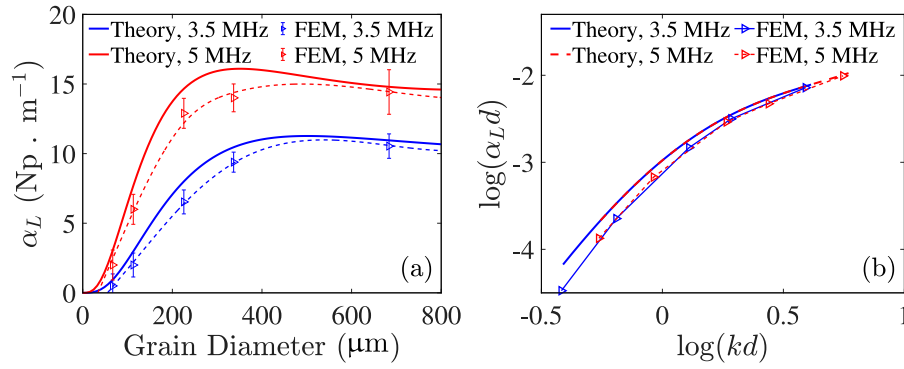


**Fig. 9.** Effect of grain size on the attenuation coefficient in (a) the linear space and (b) the normalized log space. The finite element results are compared with the theory. The error bars in (a) represent the standard deviation of attenuation values for multiple realizations corresponding to each grain size. The dashed lines in (a) are the shape-preserving fit of the discrete point (triangle markers) for better visualization. The log space plot of the normalized attenuation  $\alpha_L d$  against normalized propagation constant  $kd$  is shown in (b), where  $k$  is the wave number, and  $d$  denotes the average grain diameter.

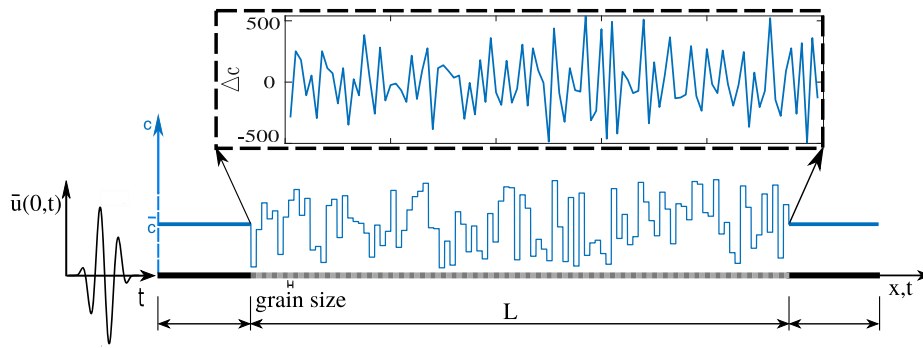


**Fig. 10.** Sketch of the computational domain representing the polycrystalline microstructure of ice. The lower plot shows the values of the speed of sound associated with each one of the grains. The upper plot records the corresponding discrete jump between one grain and the next, fundamental in our analysis of attenuation predictability. The values used in this figure correspond to one single example. We apply several permutations of the grains to achieve multiple realizations with different orderings.

distributions we use have a mean of  $916.8 \text{ kg/m}^3$  and a range between 826 and  $1234 \text{ kg/m}^3$ .

Typical material formation processes tend to develop microstructures with properties that vary, approximating normal or log-normal distributions [72,73]. In our algorithm, which reproduces variations in density, these patterns have a high probability of occurrence and do not lead to hierarchical orderings at a mesoscale. In consequence, different patterns in this category converge to similar density gradient averaged values, and the attenuation response can be predicted using a simple descriptor (e.g., mean and deviation of the distribution). However, if more extreme ordered configurations are introduced, we observe a disparity of attenuation coefficients that prevents the prediction using classical descriptors (see inset plot in Fig. 11).

We then proceed to analyze the landscape of hierarchical orderings with the objective of finding a reduced-order model to predict attenuation in complex distributions. We use an algorithm using random and specific customized parameters and subsequent permutations to generate a large number  $N_c$  of mesoscale ordered distributions of the sound speed vector  $\mathbf{c}$ . Our objective is to determine a suitable second-order descriptor that captures the attenuation variability when a particular set of grains. For each configuration  $J$  in  $N_c$ , and since the attenuation is related to interface jumps at the local level, we propose to part from a jump variable  $\Delta c$ , which we define for each  $i$  grain as:

$$\Delta c_i = c_{i+1} - c_i, \quad i = 1, \dots, N_{gr} - 1, \quad (35)$$

where  $N_{gr}$  is the total number of grains (which is kept constant between configurations). The standard deviation of particular configuration  $J$  can be expressed as:

$$\sigma_{\Delta c}^J = \sqrt{\frac{1}{N_{gr} - 1} \sum_{i=1}^{N_{gr}-1} (\Delta c_i - \overline{\Delta c}^J)^2}, \quad (36)$$

and the global average for  $J$  is computed as:

$$\overline{\Delta c}^J = \sum_{i=1}^{N_{gr}-1} \frac{\Delta c_i}{N_{gr} - 1}. \quad (37)$$

From here, we deduce a normalized second-order descriptor based on this discrete material gradient variable that allows us to quantify the ordering degree of a particular distribution. We define the variable  $\xi$  for a particular distribution  $J$  as:

$$\xi = \frac{\sigma_{\Delta c}^J}{\max(\sigma_{\Delta c}) - \min(\sigma_{\Delta c})}, \quad (38)$$

where  $\max(\sigma_{\Delta c})$  and  $\min(\sigma_{\Delta c})$  have been used for normalization, and they correspond to the maximum/minimum values of the considered spectrum of configurations ( $J = 1 \dots N_c$ ). Note that  $\xi$  describes how the jumps in material properties are distributed, and any dependence we find will not be modified by the normalization. However, in this way  $\xi$  indicates the level of organization for a particular configuration spectrum. For example, given a range of variability and a number of grains, values of  $\xi$  close to zero indicate the ordering that minimizes differences in material properties between adjacent grains, while values of  $\xi$  close to one indicate the orderings at which the magnitude of the jumps between the grains has been maximized. Our results using this parameter indicate that  $\xi$  is able to predict the attenuation coefficients for highly-ordered distributions. We present in Fig. 11 a collection of 130 different simulations on the  $\alpha_L - \xi$  space. Typical randomized configurations, such as the ones found in natural microstructures, have the highest probability of occurrence and present values in the range of  $\xi = 0.38\text{--}0.45$  (in color green). The corresponding attenuation coefficient values fall within the ranges predicted in Section 3.2, which worked with conventional distributions.

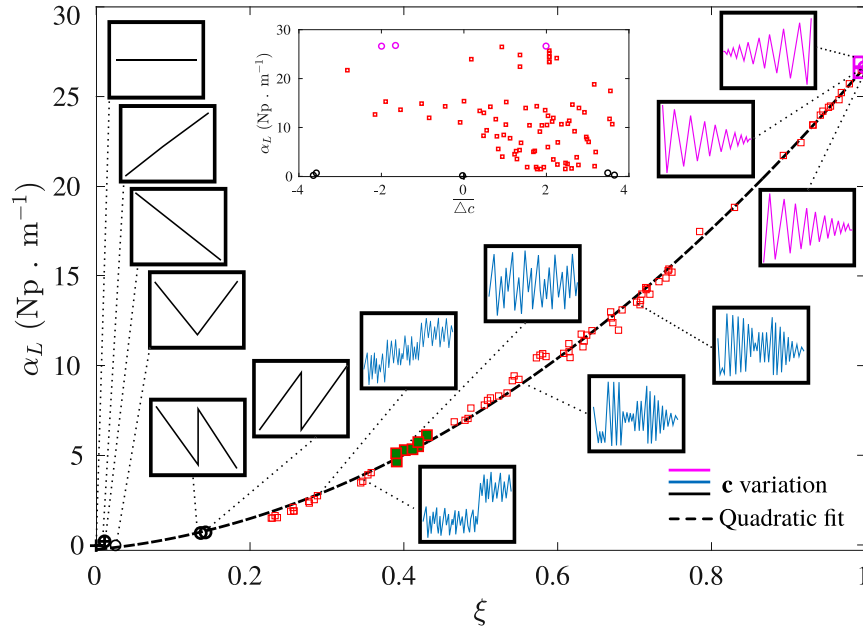


**Fig. 11.** Attenuation coefficient relationship with  $\xi$  at the frequency 3.5 MHz for 130 configurations. The top figure shows the attenuation as a function of the first-order descriptor  $\Delta c$ , which cannot capture the attenuation behavior. Each box contains a specific distribution of the speed wave  $c$ . Boxes in black mean big jumps between adjacent properties of grains, boxes in magenta mean big jumps between adjacent properties of grains, and boxes in blue mean random permutation of grains properties. The square markers in green mean random permutation with a higher probability of occurrence.

On the left side of the chart, small  $\xi$  values signal configurations that minimize the gradient of density. These types of configurations can naturally occur due to atypical growing processes or due to gravity effects. An example would be a distribution in which the speed of sound evolves from lowest to highest (or, interestingly, the other way around). It is important to note that this arrangement of material properties leads to extremely small attenuation values, far below what is expected for a random permutation of the very same values. In contrast, high values of  $\xi$  represent configurations where the gradients between grains are maximized, and lead to very high values of attenuation. These extreme lower and higher  $\xi$  configurations have been selected at random to create a representative curve and study the behavior of the attenuation over a relevant spectrum of orderings. Relevant for templating and design of artificial microstructures, these distributions exhibit unusually high attenuation values.

In conclusion, Fig. 11 shows that the relationship between attenuation and the spectrum of configurations can be reduced to a single parameter. The results of our analysis indicate that the attenuation exhibits a quadratic growth as the parameter  $\xi$  increases.

#### 3.4. Role of interface gradient in two-dimensional microstructures

In this section, we characterize the attenuation coefficient response in 2D ordered configurations. The 2D configurations implement the corresponding randomized crystal orientations. Following the methodology outlined in Section 3.3, we apply here a mass density gradient to the microstructure in the wave propagation direction  $l_x$ . We choose a computational domain with dimensions  $l_x \times l_y = 40 \times 20$  mm<sup>2</sup> that contains a total of 1000 grains. The mean grain diameter for this setup is approximately 1 mm. We then consider a random Gaussian distribution of the density that has the mean equal to the density value used in other sections of this study, namely  $\rho = 916.8$  kg/m<sup>3</sup>. Furthermore, the standard deviation of the density pattern is 26.19 kg/m<sup>3</sup> that corresponds to a 183.36 kg/m<sup>3</sup> range in density values (i.e., 20% total density change, see Fig. 12(f)). This random density distribution is utilized to generate various ordered density patterns based on parameter  $\xi$  (see Fig. 12(a–e)). We then obtain the attenuation values following the procedure explained in Section 3.1 for a 5 MHz center frequency input signal.

Different density distributions defined by the parameter  $\xi$  are shown in Fig. 12. To isolate the effect of the mass density change from the one introduced by the grain orientations, we normalize the calculated  $\alpha_L$  with respect to a baseline attenuation coefficient  $\bar{\alpha}_L$ . The baseline attenuation corresponds to the case in which the mass density is constant throughout the domain and the loss in wave amplitude is only due to the scatter resulting from different grain orientations. As can be observed in Fig. 12, the attenuation behavior is in agreement with the one obtained for 1D. Interestingly, the quadratic fit is reproduced in the two-dimensional case and the results suggest that  $\xi$  can be used as a design parameter to achieve extremely lower or higher attenuation values in realistic microstructures.

#### 4. Conclusions

In this paper, we have presented a numerical approach for the analysis of ultrasonic wave propagation in polycrystalline solids exhibiting hierarchical distributions at the mesoscale. Due to its relevance to cryoultrasonics NDE and several other fields in science and engineering, we have focused on ice as a model for this family of microstructures. We have used an optimized numerical approach to explore how attenuation within the ultrasonic frequency range is affected by a landscape of density distributions with different degrees of hierarchical ordering. We have concluded that second-ordering descriptors are necessary to accurately capture the attenuation response; moreover, we introduced a new parameter, based on the standard deviation of the speed of sound gradient, that shows a quadratic response with ultrasonic attenuation. We have tested the parameter in both one and two-dimensional settings.

Additionally, we extensively tested our computational approach and explored the numerical performance of first and second-order finite elements, and LME approximants, which cannot be found in the literature. We have concluded that (1) second-order finite elements perform better with non-optimal time step coefficients, that (2) if the optimal coefficient can be achieved, linear finite elements exhibit superior convergence, and that (3) LME stabilizes the totality of the convergence curve for the error in total energy and  $L_2$ -norm, and that, in contrast with FEM, the error decreases monotonically with the time

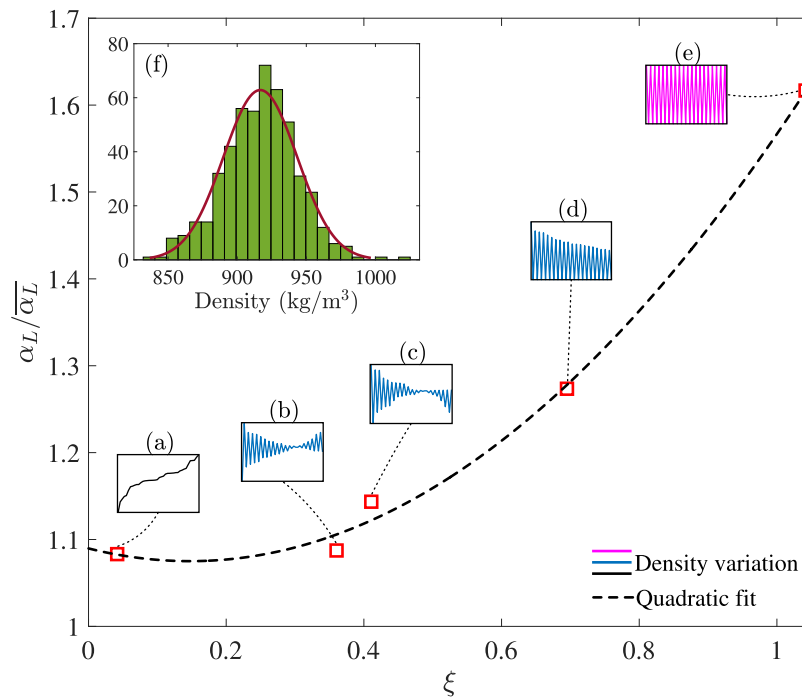


**Fig. 12.** Change in the longitudinal attenuation coefficient as a function of density variation between adjacent grains along the length of the domain  $l_x$  (i.e., the propagation direction). The vertical axis is normalized with respect to the baseline attenuation,  $\bar{\alpha}_L$ , in which density is constant throughout the domain. The density variation orderings shown in (a)–(e) are based on the random Gaussian density distribution shown in (f).

step. We have reported the upper bound for the optimal time step coefficient  $\chi \leq 0.7$  and details on the discretization parameters that achieve optimal computational performance in linear FEM.

These results are relevant for ice, for which literature is scarce, but also for any material that undergoes non-uniform growing processes that induce hierarchical organizations of material properties. Understanding wave propagation in ice opens the door to metamaterial design guidelines, where the fine-scale can be controlled precisely to obtain a customized ultrasonic response. Although 2D simulations have been proven to be representative of wave propagation of polycrystalline materials, we suggest that future work should include a validation of these results in the 3D setting. Likewise, the parameter space is large and the effect of further frequencies and grain shape should be analyzed in the frame of highly ordered configurations.

#### Declaration of competing interest

The authors declare that they have no known competing financial interests or personal relationships that could have appeared to influence the work reported in this paper.

#### Data availability

Data will be made available on request.

#### Acknowledgments

This material is based upon work supported by the National Science Foundation, United States under Grant No. 2029142. Any opinions, findings, and conclusions or recommendations expressed in this material are those of the authors and do not necessarily reflect the views of the National Science Foundation. E. Rodriguez and D. Millán wish to thank CONICET and grant L020-T1-2022 from SIIP UNCuyo. The two-dimensional simulations for this research were performed on the Pennsylvania State University's Institute for Computational and Data Sciences' Roar supercomputer. All authors approved the version of the manuscript to be published.

#### References

- [1] S. Hirsekorn, Elastic properties of polycrystals: A review, *Textures Microstruct.* 12 (1990) 1–14, <http://dx.doi.org/10.1155/TSM.12.1>.
- [2] I. Benedetti, F. Barbe, Modelling polycrystalline materials: An overview of three-dimensional grain-scale mechanical models, *J. Multiscale Model.* 05 (01) (2013) 1350002, <http://dx.doi.org/10.1142/s1756973713500029>.
- [3] S. Deville, E. Saiz, R.K. Nalla, A.P. Tomsia, Freezing as a path to build complex composites, *Science* 311 (5760) (2006) 515–518, <http://dx.doi.org/10.1126/science.1120937>, [arXiv:https://www.science.org/doi/pdf/10.1126/science.1120937](https://www.science.org/doi/pdf/10.1126/science.1120937).
- [4] S.C. Cao, J. Liu, L. Zhu, L. Li, M. Dao, J. Lu, R.O. Ritchie, Nature-inspired hierarchical steels, *Sci. Rep.* 8 (1) (2018) 5088, <http://dx.doi.org/10.1038/s41598-018-23358-7>.
- [5] F. Greco, L. Filice, C. Peco, M. Arroyo, A stabilized formulation with maximum entropy meshfree approximants for viscoplastic flow simulation in metal forming, *Int. J. Mater. Form.* 8 (3) (2015) 341–353, <http://dx.doi.org/10.1007/s12289-014-1167-x>.
- [6] C. Peco, W. Chen, Y. Liu, M.M. Bandi, J.E. Dolbow, E. Fried, Influence of surface tension in the surfactant-driven fracture of closely-packed particulate monolayers, *Soft Matter* 13 (35) (2017) 5832–5841, <http://dx.doi.org/10.1039/c7sm01245d>, [arXiv:1706.08729](https://arxiv.org/abs/1706.08729).
- [7] C. Peco, Y. Liu, C. Rhea, J.E. Dolbow, Models and simulations of surfactant-driven fracture in particle rafts, *Int. J. Solids Struct.* 156–157 (2019) 194–209, <http://dx.doi.org/10.1016/j.ijsolstr.2018.08.014>.
- [8] F. Ghanbari, F. Costanzo, D.P. Hughes, C. Peco, Phase-field modeling of constrained interactive fungal networks, *J. Mech. Phys. Solids* 145 (2020) 104160, <http://dx.doi.org/10.1016/j.jmps.2020.104160>.
- [9] Y. Liu, L.J. Bond, H. Hu, Ultrasonic-attenuation-based technique for ice characterization pertinent to aircraft icing phenomena, *AIAA J.* 55 (5) (2017) 1602–1609, <http://dx.doi.org/10.2514/1.J055500>.
- [10] P. Price, Attenuation of acoustic waves in glacial ice and salt domes, *J. Geophys. Res.: Solid Earth* 111 (2006).
- [11] C. McCarthy, R.F. Cooper, Tidal dissipation in creeping ice and the thermal evolution of Europa, *Earth Planet. Sci. Lett.* 443 (2016) 185–194, <http://dx.doi.org/10.1016/j.epsl.2016.03.006>, URL <http://dx.doi.org/10.1016/j.epsl.2016.03.006>.
- [12] M. Wang, L.F. Fan, X.L. Du, Effects of the gradient distribution of microdefects on wave propagation through a rock mass, *Int. J. Rock Mech. Min. Sci.* 154 (July 2021) (2022) <http://dx.doi.org/10.1016/j.ijrmms.2022.105125>.
- [13] F.E. Stanke, G.S. Kino, A unified theory for elastic wave propagation in polycrystalline materials, *J. Acoust. Soc. Am.* 75 (3) (1984) 665–681, <http://dx.doi.org/10.1121/1.390577>, URL <http://asa.scitation.org/doi/10.1121/1.390577>.

- [14] R.L. Weaver, Diffusivity of ultrasound in polycrystals, *J. Mech. Phys. Solids* 38 (1) (1990) 55–86, [http://dx.doi.org/10.1016/0022-5096\(90\)90021-U](http://dx.doi.org/10.1016/0022-5096(90)90021-U), URL <https://www.sciencedirect.com/science/article/pii/002250969090021U>.
- [15] M. Calvet, L. Margerin, Velocity and attenuation of scalar and elastic waves in random media: A spectral function approach, *J. Acoust. Soc. Am.* 131 (3) (2012) 1843–1862, <http://dx.doi.org/10.1121/1.3682048>, URL <http://asa.scitation.org/doi/10.1121/1.3682048>.
- [16] S.I. Rokhlin, J. Li, G. Sha, Far-field scattering model for wave propagation in random media, *J. Acoust. Soc. Am.* 137 (5) (2015) 2655–2669, <http://dx.doi.org/10.1121/1.4919333>.
- [17] C.M. Kube, J.A. Turner, Acoustic attenuation coefficients for polycrystalline materials containing crystallites of any symmetry class, *J. Acoust. Soc. Am.* 137 (6) (2015) EL476–EL482, <http://dx.doi.org/10.1121/1.4921676>, URL <http://dx.doi.org/10.1121/1.4921676>.
- [18] G. Sha, M. Huang, M.J.S. Lowe, S.I. Rokhlin, Attenuation and velocity of elastic waves in polycrystals with generally anisotropic grains: Analytic and numerical modeling, *J. Acoust. Soc. Am.* 147 (4) (2020) 2442, <http://dx.doi.org/10.1121/10.0001087>.
- [19] S. Hirsekorn, The scattering of ultrasonic waves in polycrystalline materials with texture, *J. Acoust. Soc. Am.* 77 (3) (1985) 832–843, <http://dx.doi.org/10.1121/1.392052>, URL <http://asa.scitation.org/doi/10.1121/1.392052>.
- [20] J.A. Turner, Elastic wave propagation and scattering in heterogeneous, anisotropic media: Textured polycrystalline materials, *J. Acoust. Soc. Am.* 106 (2) (1999) 541–552, <http://dx.doi.org/10.1121/1.427024>.
- [21] S. Ahmed, R.B. Thompson, Attenuation of ultrasonic waves in cubic metals having elongated, oriented grains, *Nondestruct. Test. Eval.* 8–9 (1–6) (1992) 525–531, <http://dx.doi.org/10.1080/10589759208952729>.
- [22] L. Yang, O.I. Lobkis, S.I. Rokhlin, Shape effect of elongated grains on ultrasonic attenuation in polycrystalline materials, *Ultrasonics* 51 (6) (2011) 697–708, <http://dx.doi.org/10.1016/j.ultras.2011.02.002>.
- [23] G. Ghoshal, J.A. Turner, Numerical model of longitudinal wave scattering in polycrystals, *IEEE Trans. Ultrason. Ferroelectr. Freq. Control* 56 (7) (2009) 1419–1428, <http://dx.doi.org/10.1109/TUFFC.2009.1197>.
- [24] A. Van Pamel, C.R. Brett, P. Huthwaite, M.J.S. Lowe, Finite element modelling of elastic wave scattering within a polycrystalline material in two and three dimensions, *J. Acoust. Soc. Am.* 138 (4) (2015) 2326–2336, <http://dx.doi.org/10.1121/1.4931445>, URL <http://dx.doi.org/10.1121/1.4931445>.
- [25] M. Huang, G. Sha, P. Huthwaite, S.I. Rokhlin, M.J.S. Lowe, Elastic wave velocity dispersion in polycrystals with elongated grains: Theoretical and numerical analysis, *J. Acoust. Soc. Am.* 148 (6) (2020) 3645, <http://dx.doi.org/10.1121/10.0002916>.
- [26] M. Ryzy, T. Grabec, P. Sedláč, I.A. Veres, Influence of grain morphology on ultrasonic wave attenuation in polycrystalline media with statistically equiaxed grains, *J. Acoust. Soc. Am.* 143 (1) (2018) 219, <http://dx.doi.org/10.1121/1.5020785>.
- [27] T. Grabec, I.A. Veres, M. Ryzy, Surface acoustic wave attenuation in polycrystals: Numerical modeling using a statistical digital twin of an actual sample, *Ultrasonics* 119 (June 2021) (2022) 106585, <http://dx.doi.org/10.1016/j.ultras.2021.106585>.
- [28] R. Quey, L. Renversade, Optimal polyhedral description of 3D polycrystals: Method and application to statistical and synchrotron X-ray diffraction data, *Comput. Methods Appl. Mech. Engrg.* 330 (2018) 308–333, <http://dx.doi.org/10.1016/j.cma.2017.10.029>, URL <https://www.sciencedirect.com/science/article/pii/S0045782517307028>.
- [29] P.E. Lhuillier, B. Chassignole, M. Oudaa, S.O. Kerhervé, F. Rupin, T. Fouquet, Investigation of the ultrasonic attenuation in anisotropic weld materials with finite element modeling and grain-scale material description, *Ultrasonics* 78 (2017) 40–50, <http://dx.doi.org/10.1016/j.ultras.2017.03.004>.
- [30] M. Norouziyan, S. Islam, J.A. Turner, Influence of microstructural grain-size distribution on ultrasonic scattering, *Ultrasonics* 102 (2020) 106032.
- [31] M. Groeber, M. Jackson, DREAM.3D: A digital representation environment for the analysis of microstructure in 3D, *Integr. Mater. Manuf. Innov.* 3 (2014) 56–72.
- [32] M. Arroyo, M. Ortiz, Local maximum-entropy approximation schemes: a seamless bridge between finite elements and meshfree methods, *Internat. J. Numer. Methods Engrg.* 65 (13) (2006) 2167–2202.
- [33] L. Adler, J.H. Rose, C. Mobley, Ultrasonic method to determine gas porosity in aluminum alloy castings: Theory and experiment, *J. Appl. Phys.* 59 (2) (1986) 336–347, <http://dx.doi.org/10.1063/1.336689>, URL <http://aip.scitation.org/doi/10.1063/1.336689>.
- [34] J.-M. Baik, R.B. Thompson, Ultrasonic scattering from imperfect interfaces: A quasi-static model, *J. Nondestruct. Eval.* 4 (3) (1984) 177–196, <http://dx.doi.org/10.1007/BF00566223>.
- [35] L.W. Koester, C. Zuhlke, D. Alexander, A.J. Fuller, B.M. Wilson, J.A. Turner, Near-race ultrasonic detection of subsurface defects in bearing rings, in: *Bearing Steel Technologies*, 9th Volume, in: ASTM Special Technical Publication, ASTM International, 2012, pp. 84–101, <http://dx.doi.org/10.1520/STP104623>.
- [36] A.P. Arguelles, J.A. Turner, Ultrasonic attenuation of polycrystalline materials with a distribution of grain sizes, *J. Acoust. Soc. Am.* 141 (6) (2017) 4347–4353.
- [37] F. Simonetti, M. Fox, Experimental methods for ultrasonic testing of complex-shaped parts encased in ice, *NDT & E Int.* 103 (2019) 1–11, <http://dx.doi.org/10.1016/j.ndteint.2019.01.008>, URL <http://www.sciencedirect.com/science/article/pii/S0963869518306376>.
- [38] F. Simonetti, I.L. Satow, A.J. Brath, K.C. Wells, J. Porter, B. Hayes, K. Davis, Cryo-ultrasonic NDE: Ice-cold ultrasonic waves for the detection of damage in complex-shaped engineering components, *IEEE Trans. Ultrason. Ferroelectr. Freq. Control* 65 (4) (2018) 638–647, <http://dx.doi.org/10.1109/TUFFC.2018.2796387>.
- [39] K.F. Voikovskii, Translation of The Mechanical Properties of Ice, 1960, URL <https://apps.dtic.mil/dtic/tr/fulltext/u2/284777.pdf>.
- [40] M.J. Vaughan, K.V. Wijk, D.J. Prior, M.H. Bowman, Monitoring the temperature-dependent elastic and anelastic properties in isotropic polycrystalline ice using resonant ultrasound spectroscopy, 2016, pp. 2821–2829, <http://dx.doi.org/10.5194/tc-10-2821-2016>.
- [41] C.J. Permann, D.R. Gaston, D. Andriš, R.W. Carlsen, F. Kong, A.D. Lindsay, J.M. Miller, J.W. Peterson, A.E. Slaughter, R.H. Stogner, R.C. Martineau, MOOSE: Enabling massively parallel multiphysics simulation, *SoftwareX* 11 (2020) 100430, <http://dx.doi.org/10.1016/j.softx.2020.100430>, URL <http://www.sciencedirect.com/science/article/pii/S2352711019302973>.
- [42] K.-J. Bathe, Finite Element Procedures, Klaus-Jurgen Bathe, 2006.
- [43] G. Seriani, S. Oliveira, Numerical modeling of mechanical wave propagation, *La Rivista Del Nuovo Cimento* 43 (9) (2020) 459–514.
- [44] N.M. Newmark, A method of computation for structural dynamics, *J. Eng. Mech.* 85 (EM3) (1959) 67–94.
- [45] J. Petrovic, Review mechanical properties of ice and snow, *J. Mater. Sci.* 38 (1) (2003) 1–6.
- [46] T. Hughes, J. Cottrell, Y. Bazilevs, Isogeometric analysis: CAD, finite elements, NURBS, exact geometry and mesh refinement, *Comput. Methods Appl. Mech. Engrg.* 194 (2005) 4135–4195.
- [47] Y. Bazilevs, V. Calo, J. Cottrell, J. Evans, T. Hughes, S. Lipton, M. Scott, T. Sederberg, Isogeometric analysis using T-splines, *Comput. Methods Appl. Mech. Engrg.* 199 (5–8) (2010) 229–263.
- [48] A. Rosolen, M. Arroyo, Blending isogeometric analysis and local maximum entropy meshfree approximants, *Comput. Methods Appl. Mech. Engrg.* 264 (2013) 95–107.
- [49] D. Millán, A. Rosolen, M. Arroyo, Thin shell analysis from scattered points with maximum-entropy approximants, *Internat. J. Numer. Methods Engrg.* 85 (6) (2011) 723–751.
- [50] D. Millán, A. Rosolen, M. Arroyo, Nonlinear manifold learning for meshfree finite deformation thin-shell analysis, *Internat. J. Numer. Methods Engrg.* 93 (7) (2013) 685–713.
- [51] A. Rosolen, C. Peco, M. Arroyo, An adaptive meshfree method for phase-field models of biomembranes. Part I: Approximation with maximum-entropy basis functions, *J. Comput. Phys.* 249 (2013) 303–319, <http://dx.doi.org/10.1016/j.jcp.2013.04.046>.
- [52] C. Peco, A. Rosolen, M. Arroyo, An adaptive meshfree method for phase-field models of biomembranes. Part II: A Lagrangian approach for membranes in viscous fluids, *J. Comput. Phys.* 249 (2013) 320–336.
- [53] T. Belytschko, Y.Y. Lu, L. Gu, Element-free Galerkin methods, *Internat. J. Numer. Methods Engrg.* 37 (2) (1994) 229–256.
- [54] W.K. Liu, S. Jun, Y.F. Zhang, Reproducing kernel particle methods, *Internat. J. Numer. Methods Fluids* 20 (8–9) (1995) 1081–1106.
- [55] A. Rosolen, D. Millán, M. Arroyo Balaguer, On the optimum support size in meshfree methods: a variational adaptivity approach with maximum-entropy approximants, *Internat. J. Numer. Methods Engrg.* 82 (7) (2010) 868–895.
- [56] C. Peco, D. Millán, A. Rosolen, M. Arroyo, Efficient implementation of Galerkin meshfree methods for large-scale problems with an emphasis on maximum entropy approximants, *Comput. Struct.* 150 (2015) 52–62, <http://dx.doi.org/10.1016/j.compstruc.2014.12.005>.
- [57] D. Millán, N. Sukumar, M. Arroyo, Cell-based maximum-entropy approximants, *Comput. Methods Appl. Mech. Engrg.* 284 (2015) 712–731.
- [58] J. Zhang, J. Brown, S. Balay, J. Faibussowitsch, M. Knepley, O. Marin, R.T. Mills, T. Munson, B.F. Smith, S. Zampini, The PetscSF scalable communication layer, *IEEE Trans. Parallel Distrib. Syst.* 33 (4) (2022) 842–853.
- [59] S. Balay, S. Abhyankar, M.F. Adams, S. Benson, J. Brown, P. Brune, K. Buschelman, E.M. Constantinescu, L. Dalcin, A. Dener, V. Eijkhout, W.D. Gropp, V. Hapla, T. Isaac, P. Jolivet, D. Karpeev, D. Kaushik, M.G. Knepley, F. Kong, S. Kruger, D.A. May, L.C. McInnes, R.T. Mills, L. Mitchell, T. Munson, J.E. Roman, K. Rupp, P. Sanan, J. Sarich, B.F. Smith, S. Zampini, H. Zhang, H. Zhang, J. Zhang, PETSc Web page, 2022, <https://petsc.org/>. URL <https://petsc.org/>.
- [60] The pennsylvania state university's institute for computational and data sciences' roar super computer, 2022, <https://www.icds.psu.edu/computing-services/system-specifications/>.
- [61] R. Quey, P. Dawson, F. Barbe, Large-scale 3D random polycrystals for the finite element method: Generation, meshing and remeshing, *Comput. Methods Appl. Mech. Engrg.* 200 (17–20) (2011) 1729–1745.
- [62] A. Prakash, D. Weygand, E. Bitzek, Influence of grain boundary structure and topology on the plastic deformation of nanocrystalline aluminum as studied by atomistic simulations, *Int. J. Plast.* 97 (2017) 107–125.



- [63] S. Falco, J. Jiang, F. De Cola, N. Petrinic, Generation of 3D polycrystalline microstructures with a conditioned Laguerre-Voronoi tessellation technique, *Comput. Mater. Sci.* 136 (2017) 20–28.
- [64] X. Zheng, T. Sun, J. Zhou, R. Zhang, P. Ming, Modeling of polycrystalline material microstructure with 3D grain boundary based on Laguerre-Voronoi tessellation, *Materials* 15 (6) (2022) 1996.
- [65] A. Van Pamel, G. Sha, S.I. Rokhlin, M.J. Lowe, Finite-element modelling of elastic wave propagation and scattering within heterogeneous media, *Proc. R. Soc. A* 473 (2197) (2017) 20160738.
- [66] A.A. Elvin, Number of grains required to homogenize elastic properties of polycrystalline ice, *Mech. Mater.* 22 (1) (1996) 51–64.
- [67] M. Ortiz, B. Nour-Omid, E.D. Sotelino, Accuracy of a class of concurrent algorithms for transient finite element analysis, *Internat. J. Numer. Methods Engrg.* 26 (2) (1988) 379–391, <http://dx.doi.org/10.1002/nme.1620260207>, arXiv: <https://onlinelibrary.wiley.com/doi/pdf/10.1002/nme.1620260207>. URL <https://onlinelibrary.wiley.com/doi/abs/10.1002/nme.1620260207>.
- [68] H.P. Langtangen, S. Linge, *Finite Difference Computing with PDEs: A Modern Software Approach*, Springer Nature, 2017.
- [69] A.N. Kalashnikov, R.E. Challis, Errors and uncertainties in the measurement of ultrasonic wave attenuation and phase velocity, *IEEE Trans. Ultrason. Ferroelectr. Freq. Control* 52 (10) (2005) 1754–1768.
- [70] A. Van Pamel, C.R. Brett, P. Huthwaite, M.J. Lowe, Finite element modelling of elastic wave scattering within a polycrystalline material in two and three dimensions, *J. Acoust. Soc. Am.* 138 (4) (2015) 2326–2336.
- [71] A. Van Pamel, G. Sha, S.I. Rokhlin, M.J.S. Lowe, Finite-element modelling of elastic wave propagation and scattering within heterogeneous media, *Proc. R. Soc. A* 473 (2197) (2017) 20160738, <http://dx.doi.org/10.1098/rspa.2016.0738>, URL <https://royalsocietypublishing.org/doi/abs/10.1098/rspa.2016.0738>.
- [72] J.C. Tucker, L.H. Chan, G.S. Rohrer, M.A. Groeber, A.D. Rollett, Tail departure of log-normal grain size distributions in synthetic three-dimensional microstructures, *Metall. Mater. Trans. A* 43 (8) (2012) 2810–2822.
- [73] J. Heintzenberg, Properties of the log-normal particle size distribution, *Aerosol Sci. Technol.* 21 (1) (1994) 46–48.